Regularization of discrete contour by Willmore energy

E. Bretin [*], J.-O. Lachaud [†], É. Oudet [‡]

1   Introduction

Shapes which minimize their total squared curvature have risen a lot of interest in the mathematics community. In the 2D plane, they are known as Euler elastica ([6], [17]), while its 3D variant is the minimization of the Willmore energy ([28], [27]) and has lead to the Willmore conjecture [30]. Such shapes have nice properties (smoothness, sphericity) and arise in different fields of mathematical modeling (deformation of thin plate, waving of a snake, red blood cells), computer vision and image analysis (e.g. see the famous deformable models [19]).

Recently, Kerautret and Lachaud [20, 21] proposed to use these shapes for reconstructing a continuous analog to digital shapes. The idea is to find among all possible euclidean shapes that have the same digitization as the digital shape of interest, the one with smallest total squared curvature. In a sense, due to its smoothness and invariance properties, this euclidean shape is a very natural one with the desired digitization. By this way, they obtain a curvature estimator with many desirable properties (accuracy, stability, robustness to noise).

In their paper, the authors solve an approximate version of this problem. The family of shapes is restricted to compact simply connected shapes of $\mathbb{R}^2$ with boundary made of circular arcs with tangent continuity. Furthermore, the digitization constraint is not exactly enforced but only approached.

In this paper, we propose two others methods to address this problem, each one having its advantages and drawbacks. The first one uses the support function of convex sets [29]. It is limited to the reconstruction of convex digital shapes, satisfies exactly the digitization constraints, is simple to implement and relatively fast. Due to its proved reliability, we use this method to assess the second one. However its restriction to convex shapes limits its role in practical applications.

The second more flexible method is related to phase field approaches [1, 4]. It can reconstruct arbitrary digital shapes, satisfies the digitization constraint up to a given error bound, but is slower. These two methods are finely compared. The second one is also

---

[*]CMAP, Ecole Polytechnique, 91128 Palaiseau, France.
`bretin@polytechnique.fr`

[†]Laboratoire de mathématiques, Université de Savoie, Campus scientifique, 73376 Le Bourget-du-lac, France. `jacques-olivier.lachaud@univ-savoie.fr`
`http://www.lama.univ-savoie.fr/~lachaud`

[‡]Laboratoire de mathématiques, Université de Savoie, Campus scientifique, 73376 Le Bourget-du-lac, France. `Edouard.Oudet@univ-savoie.fr`
`http://www.lama.univ-savoie.fr/~oudet`

compared to the original method proposed in [20, 21], in order to evaluate the accuracy of this approximated solution with respect to curvature estimates.

Before presenting the three methods, we state precisely our problem. A *digital object* O is a non-empty finite subset of $\mathbb{Z}^2$. To simplify the exposition, the object O will also be considered 4-connected, with its complement in $\mathbb{Z}^2$ 8-connected. Such digital object are often called *polyominoes*. Their digital contour is a simple 4-connected curve in the half-integer plane. We consider the family $\mathbb{F}$ of simply connected compact shapes in $\mathbb{R}^2$, whose boundary is rectifiable and whose curvature map is in L^2. This constraint avoids fractal-like shapes and the curvature, while not compulsory defined everywhere, is therefore square integrable. By definition, the *topological boundary* of a subset X of $\mathbb{R}^2$ is the subset of $\mathbb{R}^2$ defined as the closure of X minus its interior. We denote it by ∂X further on. Considering the properties of the family $\mathbb{F}$ the boundary of its elements are simple closed curves of the plane. Finally, let $\mathrm{Dig} : \mathcal{P}(\mathbb{R}^2) \to \mathbb{Z}^2$ be the Gauss digitization process, i.e. $\mathrm{Dig}(X) = X \cap \mathbb{Z}^2$.

We are only interested in Euclidean shapes that have the same digitization as the digital object O. We therefore consider the family

$$\mathbb{F}(O) = \{X \in \mathbb{F}, \mathrm{Dig}(\underbrace{X \setminus \partial X}_{\text{interior}}) \subset O \text{ and } \mathrm{Dig}(\underbrace{\mathbb{R}^2 \setminus X}_{\text{exterior}}) \subset \mathbb{Z}^2 \setminus O\}.$$

We wish to find some optimal shape solution of:

$$\inf_{X \in \mathbb{F}(O)} F(X), \quad \text{with } F(X) = \int_{\partial X} \kappa^2 d\sigma, \tag{1}$$

where κ stands for the standard curvature. Notice that the well-posedness of the previous shape optimization problem is not obvious. The existence question and the local optimality conditions will be address in a forthcoming work (see [Dorin-Jaco]).

Our paper is organized as follows. We begin in Section 2 by recalling the optimization method of [20, 21], which extracts an approximated solution to (1) and is valid for arbitrary digital object. In Section 3, we describe the first new method for solving (1), which is limited to convex shapes. Section 4 presents the second new method for solving (1), which is valid for arbitrary digital object. Section 5 presents a comparative evaluation of all three methods, in terms of accuracy and computation time. More precisely, the accuracy of the generic phase field method is assessed on convex shapes by comparison with fine results obtained by our first approach. Our experiments confirm the quality of the phase field approach. Finally, we compare the approximated curvature estimator of [20, 21] to the curvature field of the phase field reconstruction. It appears that this approximation is both good and robust while computation time are hundred times faster.

2 Digital geometry approach

This section summarizes the digital geometry approach to solve (1) [20, 21]. The idea is to extract the linear subparts of the boundary of the digital object O. Each identified linear subpart locally defines upper and lower constraints on the local slope of the Euclidean shape boundary. The optimization problem is then solved in a tangent space where the optimized contour is represented by its slopes, and not by its positions.
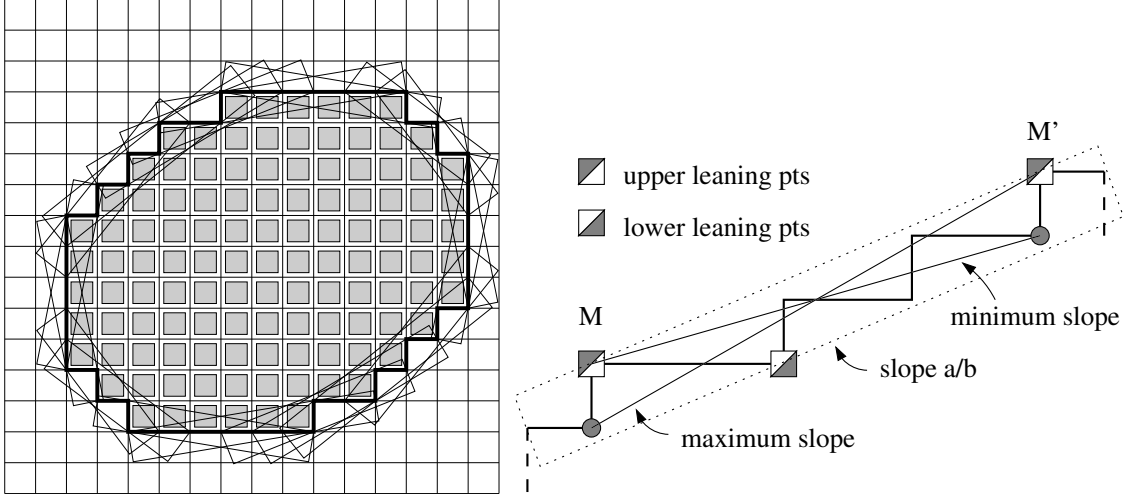
Figure 1: Left: tangential cover of the boundary of a digitized shape, where each maximal segment is drawn as a black bounding box aligned with its slope. Right: slope of a maximal segment and estimation of maximal and minimal slopes with leaning points.

More precisely, the input data is the inter-pixel boundary of some digital object, that we will call later on a *digital contour*. It is thus a 4-connected closed path C in the digital plane, whose points C_i are numbered consecutively. These points lies in the half-integer plane since pixel centers have integer coordinates. A sequence of connected points of C going in an increasing sequence of indices from C_i to C_j is conveniently denoted by $C_{i,j}$.

Such a sequence is a *digital straight segment* iff its points are included in some standard digital straight line, i.e. $\exists (a, b, \mu) \in \mathbb{Z}^3, \forall k, i \leq k \leq j, \mu \leq a x_{C_k} - b y_{C_k} < \mu + |a| + |b|$. The standard line with smallest $|a|$ and containing the sequence, defines the characteristics (a, b, μ) of the digital straight segment. In particular, the *slope* of the segment is a/b. Let us now denote by $S(i, j)$ the predicate "$C_{i,j}$ is a digital straight segment". A *maximal segment* of C is a sequence $C_{i,j}$ such that $S(i, j) \wedge \neg S(i, j+1) \wedge \neg S(i-1, j)$. The *maximal segments* are thus by definition the inextensible digital straight segments of C. Together, they constitute the *tangential cover* of C, as illustrated on Figure 1, left.

The tangential cover of a digital contour can be efficiently computed in linear time with respect to its number of points [16, 23]. The directions of maximal segments may be used to estimate the tangent direction of the underlying shape [23]. Here we also make use of the direction of maximal segments, but to estimate locally the geometries of all possible underlying shapes. We proceed as follows.

1. Each maximal segment tells us some information on the local geometry of the underlying continuous shape. In particular, the direction of maximal segment gives bounds on the possible tangent directions of the continuous shape around this place. These bounds are deduced from the upper and lower leaning points of the maximal segment (Figure 1, right).

2. We associate to every closed C^1-curve $\mathcal{C}$ parameterized by its arc length s the graph function which maps s to the tangent direction at $\mathcal{C}(s)$. The domain is $[0, |\mathcal{C}|[, |\mathcal{C}|$ being

3
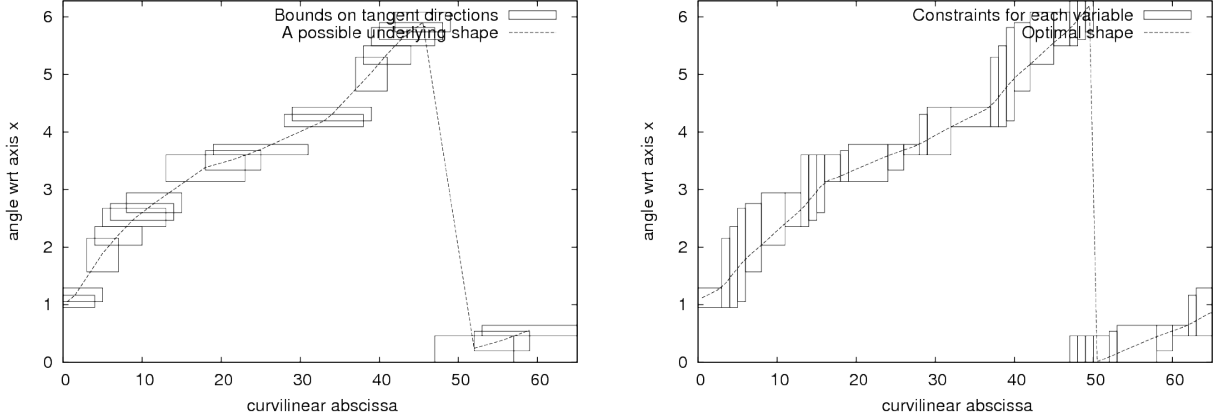
Figure 2: The shape of interest is an ellipse of semi-axes 10 and 6, rotated by 0.5 radians (see Figure 1). Left: bounds given by each maximal segment on the possible local tangent direction. A possible underlying shape should have its tangent space representation staying within these boxes. Right: Each variable has a possible range given by its vertical line. The shape that minimizes its squared curvature is represented by the dashed line.

the length of $\mathcal{C}$, and the range is $[0, 2\pi[$. Such a representation, that we call hereafter *tangent space*, defines the closed curve geometry up to a translation.

3. We fix C_0 as the starting point of the arc length parameterization. Given a digital length estimator, we can estimate the arc length s_i associated to any point C_i, and also the total perimeter LCC. For each maximal segment $C_{i,j}$, we then draw in the tangent space an axis aligned box spanning abscissas s_i to s_j and whose ordinates are the inverse tangent of the bounds determined above (Figure 2, left).

4. A curve whose tangent space representation stays within the boxes defined above defines a shape which is approximately digitized as O. The family of curves whose tangent space representation stays within the boxes is thus an approximation of $\mathbb{F}(O)$, and the subsequent optimization process will take place in this approximate family (Figure 2, right).

We therefore find the optimal shape of (1) in the tangent space representation. Finally let $t(s)$ be the tangent direction of the curve at curvilinear abscissa s. Item (4) of the preceding paragraph gives the approximate bounds $a(s)$ and $b(s)$ on the tangent direction of $\mathcal{C}$ at s. This is illustrated on Figure 2 and detailed in [21]. Solving (1) reduces to solving :

$$\min_{t:\forall s, a(s) \leq t(s) \leq b(s)} \int_0^{|\mathcal{C}|} \left(\frac{dt}{ds}\right)^2 ds, \tag{2}$$

with t a piecewise C^1-function from $[0, |\mathcal{C}|]$ to $[0, 2\pi[$, with $t(0) = t(|\mathcal{C}|)$. Let us now denote by $(i_l)_{l \in \{0..L-1\}}$ the increasing sequence of indices of the digital points that are starting or ending point of a maximal segment, and let $(s_{(i_l)})$ be the corresponding sequence of curvilinear abscissae. Looking now at an arbitrary portion $[s_{i_l}, s_{i_{l+1}}[$ of the curve, the functions a and b

4

are constant on this interval and denoted by (a_l) and (b_l). Standard variation calculus on (2) immediately gives the necessary condition $2\frac{d}{ds}\frac{dt}{ds} = 0$ when $a(s) < t(s) < b(s)$. If $t_l = t(s_l)$, then the solution in this interval is the straight segment $t(s) = t_l + \frac{t_{l+1}-t_l}{s_{i_{l+1}}-s_{i_l}}(s - s_{i_l})$. A straight segment in the tangent space is a circular arc in the plane. Equation (2) is thus reduced to the finite-dimensional optimization problem:

$$\text{Find} \quad (t_l)_{l\in\{0..L-1\}},$$

$$\text{which minimizes} \quad F(t_0,\ldots,t_{L-1}) \quad = \sum_l \left(\frac{t_{l+1}-t_l}{s_{i_{l+1}}-s_{i_l}}\right)^2 (s_{i_{l+1}} - s_{i_l}),$$

$$\text{subject to} \quad \forall l, a_l \leq t_l \leq b_l.$$

We use classical iterative numerical techniques to solve this convex optimization problem. More precisely, we optimize variables consecutively, similarly to a relaxation method (see for instance [10]). Geometrically, the tangent direction of the optimal curve is the piecewise linear function going through points (s_{i_l}, t_l). Tangent and curvature are straightforwardly obtained, while position is obtained by integration. The obtained curve is not closed in general which is a drawback if the user is interested not only by curvature estimates but also by a spatial reconstruction.

This method only approaches the solution of (1) since the bounds on tangent directions do not guarantee that the shape is in $\mathbb{F}(O)$. The length of the optimal curve is also *a priori* guessed with a length estimator, and is thus only approached. We can nevertheless notice that the length estimator is the integration of λ-MST tangent estimator [23], which is proven to be uniformly multigrid convergent to the true length in $O(h^{\frac{1}{3}})$, where h is the discretization step [22]. This method is very fast, since the number of variables to optimize is some $O(N^{\frac{2}{3}})$, if N is the number of digital points of C [11].

3   Regularization of convex contour

We present in this section a numerical approach restricted to the two dimensional convex case. More precisely, we restrict our study to the case of convex constraints and convex regularization. This strong hypothesis makes it possible to transform our regularization task into one convex optimization problem. This new formulation leads us to an efficient and reliable numerical algorithm in dimension 2.

In that simplified convex context, our regularization problem reduces to identify an optimal convex set Ω solution of:

$$\inf_{\Omega_{int}\subset\Omega\subset\Omega_{ext}} F(\Omega)$$

where Ω_{int} and Ω_{ext} are full-dimensional convex sets of the plane and

$$F(\Omega) = \int_{\partial\Omega} \kappa^2 \, d\sigma \tag{3}$$

where κ stands for the mean curvature on $\partial\Omega$. Notice that the minimization of F is equivalent to minimize the classical Willmore energy since the genus is constant in the class of convex

bodies (see [30] for a complete introduction to Willmore conjecture). To introduce our parametrization of convex sets we recall some classical definitions of convex geometry. Let Ω be a 2 dimensional convex set. We define h_Ω, *the support function* of Ω, as the function defined on the unit circle S^1 which satisfies:

$$h_\Omega(\theta) = \sup_{x \in \Omega} x \cdot \nu(\theta)$$

where $\nu(\theta) = (\cos\theta, \sin\theta)$ and the dot stands for the usual scalar product of $\mathbb{R}^2$. Notice that if $0 \in \Omega$, $h_\Omega(\theta)$ is simply the distance from the origin to the tangent line to Ω of normal direction $\nu(\theta)$. In addition, the relation of inclusion of convex sets is equivalent to the ordering of support functions. For instance in our context,

$$\Omega_{int} \subset \Omega \subset \Omega_{ext} \Leftrightarrow h_{\Omega_{int}} \leq h_\Omega \leq h_{\Omega_{ext}}. \tag{4}$$

Moreover, if h_Ω is regular enough and Ω is strictly convex such that its reverse Gauss map is well defined, it satisfies point-wise the differential equation

$$\frac{d^2 h_\Omega}{d\theta^2} + h_\Omega = R \tag{5}$$

where R is the radius of curvature at the (unique) point of $\partial\Omega$ of normal direction $\nu(\theta)$. Conversely, for any positive 2π-periodic function R which satisfies the orthogonality conditions

$$\int_0^{2\pi} R\cos\theta \, d\theta = \int_0^{2\pi} R\sin\theta \, d\theta = 0, \tag{6}$$

it exists a unique convex set $\Omega \subset \mathbb{R}^2$ (up to translations) whose support function h_Ω satisfies (5). Additionally, if h_Ω is regular enough and $R > 0$, the cost function (3) can be computed by

$$F(\Omega) = \int_0^{2\pi} \frac{1}{R} \, d\theta = \int_0^{2\pi} \left(\frac{d^2 h_\Omega}{d\theta^2} + h_\Omega \right)^{-1} d\theta. \tag{7}$$

As a consequence, solving the optimization problem (3) is equivalent to solve the convex and linear constrained problem:

$$\inf_{h_{\Omega_{int}} \leq h \leq h_{\Omega_{ext}}} \int_0^{2\pi} \left(\frac{d^2 h}{d\theta^2} + h \right)^{-1} d\theta$$

among 2π-periodic functions which satisfy $\frac{d^2 h}{d\theta^2} + h \geq 0$. This last condition ensure that h is a support function of some 2 dimensional convex set. This last remark is the starting point of our numerical approach based on a discretization by the radius of curvature.

Let $n \in \mathbb{N}^*$ be given and $(R_i)_{1 \leq i \leq n}$ be a positive vector which corresponds to the values of a step function R on $[0, 2\pi]$ associated to a subdivision $a_0 = 0 < a_1 \cdots < 2\pi = a_n$. Assume that R satisfies the orthogonality conditions (6). Every solution h of (5) has the form $A_i \cos\theta + B_i \sin\theta + R_i$ on every interval $[a_{i-1}, a_i]$ for $i = 1, \ldots, n$. Let us select one particular solution $h_{(R_i)}$ of (5) by imposing to (A_i) and (B_i) the continuity conditions of h and h' at the points $a_1, \ldots, a_{n-1}, a_n$. Under those constraints, the identification of the unknowns (A_i) and (B_i) is equivalent to solve a well posed linear system of size $2n$. In

addition, every solutions $h_{((R_i),\tau)}$ of the above differential equation can be written in the form

$$h_{((R_i),\tau)} = h_{(R_i)} + \tau . \nu(\theta) \tag{8}$$

for some $\tau \in \mathbb{R}^2$. The two additional degrees of freedom of τ correspond to the choice of a translation. With these notations the optimization problem reduces to

$$\min_{((R_i),\tau)} \sum_{i=0}^{n-1} \frac{a_{i+1} - a_i}{R_{i+1}} \tag{9}$$

under the additional constraints (6) and the infinite number of point-wise constraints

$$h_{\Omega_{int}} \leq h_{((R_i),\tau)} \leq h_{\Omega_{ext}}. \tag{10}$$

In order to obtain a finite number of constraints we relax the last condition by imposing the previous inequalities only on a discrete number of values $(\theta_j)_{1 \leq j \leq m}$ of $[0, 2\pi]$. Since the coefficients of $h_{((R_i),\tau)}$ depend linearly on the vector (R_i) this set of constraints is linear with respect to the parameters $((R_i), \tau)$. Finally we have to solve (9) under the 2 linear equalities (6) imposed on the parameters $((R_i), \tau)$, the periodic condition $R_1 = R_n$ and the $m + n$ linear inequalities associated to (10) and the positiveness of (R_i).

In order to achieve the numerical optimization procedure, we used the standard commercial software *KNITRO* (see [5]) which implements an interior/projected conjugate gradient algorithm. The stopping criterion is based on first order optimality conditions. The algorithm stops when the $||.||_\infty$ norm of the Lagrangian is less than 1e-6 times its initial value.

4 Minimization of Willmore energy via phase field method

The aim of this section is to present a phase field model adapted to the minimization of the Willmore problem:

$$\Omega^* = \underset{\Omega_{int} \subset \Omega \subset \Omega_{ext}}{\arg\min} \int_{\partial\Omega} \kappa^2 d\sigma. \tag{11}$$

Let us first recall the easier and well-known case of the approximation of mean curvature flow [15, 8, 9, 14, 1, 2] by phase field method. In this situation the interface evolves according to the gradient flow of the perimeter $P(\Omega) = \int_{\partial\Omega} 1 \, d\sigma$.

The main idea of the phase field approach is to use an approximation of the perimeter P given by the famous Ginzburg–Landau functional [25, 24]:

$$P_\epsilon(u) = \int_{\mathbb{R}^d} \left(\frac{\epsilon}{2} |\nabla u|^2 + \frac{1}{\epsilon} W(u) \right) dx, \tag{12}$$

where $\epsilon > 0$ is a small parameter, and W is a double well potential with wells locate at 0 and 1 (for example $W(s) = \frac{1}{2}s^2(1-s)^2$). Modica and Mortola [25, 24] have shown the Γ-convergence of P_ϵ to $c_W P$ in $L^1(\mathbb{R}^d)$ (see also [3]), where $c_W = \int_0^1 \sqrt{2W(s)} ds$. Roughly speaking, this result asserts that the minimization of the perimeter is equivalent to the minimization of

(12) with ε small. From a theoretical point of view, notice that, assuming the optimal shape Ω is known, then an optimal solution of (12) is provided by $u_\epsilon = q\left(\frac{\text{dist}(x,\Omega)}{\epsilon}\right)$. The associated profile function q solves the one dimensional problem

$$q = \arg\min\left\{\int_{\mathbb{R}}\left(\frac{1}{2}\gamma'^2 + W(\gamma)\right)\ ;\ \gamma \in H^1_{loc}(\mathbb{R}),\ \gamma(-\infty) = +1,\ \gamma(+\infty) = 0,\ \gamma(0) = \frac{1}{2}\right\} \quad (13)$$

and $\text{dist}(x, \Omega)$ is the signed distance function associated to Ω. This result shows that the phase field profiles are obtained by a smoothing of the distance function inversely proportional to the parameter ε.

One major difference with standard phase field approach relies in the inclusion constraints. In order to tackle this issue, we define the following penalized perimeter problem

$$P_{\Omega_{int},\Omega_{ext}}(\Omega) = \begin{cases} \int_{\partial\Omega} 1\,d\sigma & \text{if } \Omega_{int} \subset \Omega \subset \Omega_{ext} \\ +\infty & \text{otherwise} \end{cases}$$

where Ω_{int} and Ω_{ext} are two given smooth subsets of $\mathbb{R}^d$ such that $\text{dist}(\partial\Omega_{int}, \partial\Omega_{ext}) > 0$. We then introduce two continuous potentials W_{int} and W_{ext} satisfying the following assumptions :

$$(H_1)\begin{cases} W_{int}(s) = W(s) & \text{for } s \geq 1/2, \\ W_{int}(s) \geq W(s) & \text{for } s \leq 1/2, \\ W'_{int}(s) < 0 & \text{for } s < 1/2, \end{cases} \quad \text{and} \quad \begin{cases} W_{ext}(s) = W(s) & \text{for } s \leq 1/2, \\ W_{ext}(s) \geq W(s) & \text{for } s \geq 1/2, \\ W'_{ext}(s) > 0 & \text{for } s > 1/2. \end{cases}$$

Then, we denote by $P_{\epsilon,\Omega_{int},\Omega_{ext}}$ the relaxed energy:

$$P_{\epsilon,\Omega_{int},\Omega_{ext}}(u) = \int_{\mathbb{R}^d}\left[\frac{\epsilon|\nabla u|^2}{2} + \frac{1}{\epsilon}W_{\Omega_{int},\Omega_{ext}}(u, x)\right]dx,$$

where $W_{\Omega_{int},\Omega_{ext}}(s, x)$ is defined by

$$W_{\Omega_{int},\Omega_{ext}}(s, x) = \begin{cases} W_{int}(s) & \text{if } x \in \Omega_{int}, \\ W_{ext}(s) & \text{if } x \in \mathbb{R}^d \setminus \Omega_{ext}, \\ W(s) & \text{if } x \in \Omega_{ext} \setminus \Omega_{int}. \end{cases}$$

Intuitively, the previous potential forces u_ε to be asymptotically equal to 1 on Ω_{int} and 0 on Ω_{ext}. More precisely, we demonstrate in appendix A that $P_{\epsilon,\Omega_{int},\Omega_{ext}}$ Γ-converges to $c_W P_{\Omega_{int},\Omega_{ext}}$. This proof closely follows the one of [25, 24].

To study the case of Willmore's energy where $F(\Omega) = \int_{\partial\Omega}\kappa^2 d\sigma$, we consider the following approximation introduced in [13, 12]:

$$F_\epsilon(u) = \int_{\mathbb{R}^d}\frac{1}{\epsilon}\left(-\epsilon\triangle u + \frac{1}{\epsilon}W'(u)\right)^2 dx.$$

It easily follows that F_ϵ does not Γ-convergence to $c_W F$. Nevertheless, Roger and Schatzle have recently established [26] that $\Gamma - \lim_{\epsilon\to 0}(F_\epsilon + P_\epsilon) = c_W(F + P)$. Notice that

it is straightforward to deduce that, whatever the parameter $\delta > 0$, $F_\epsilon + \delta P_\epsilon$ converges to $c_W (F + \delta P)$. As a consequence we will neglect in our experiments the perimeter term applying previous result with δ small. Moreover, to deal with our additional boundary constraints, we modify F_ϵ as follows

$$F_{\epsilon,\Omega_1,\Omega_2}(u) = \int_{\mathbb{R}^d} \frac{1}{\epsilon} \left(-\epsilon \triangle u + \frac{1}{\epsilon} \partial_u W_{\Omega_{int},\Omega_{ext}}(u,x)\right)^2 dx.$$

Whereas this convergence has not been proved yet, we expect that the same ideas of the proof given in the appendix A apply and give:

$$\Gamma - \lim_{\epsilon \to 0} \left(F_{\epsilon,\Omega_{int},\Omega_{ext}} + P_{\epsilon,\Omega_{int},\Omega_{ext}}\right) = c_W \left(F + P_{\Omega_{int},\Omega_{ext}}\right).$$

We will use in the following the gradient flow of $F_{\epsilon,\Omega_{int},\Omega_{ext}}$ to approximate our optimization problem. Standard variation calculus gives the Euler-Lagrange equation which is used in our phase field formulation:

$$u_t = -\Delta^2 u + \frac{1}{\epsilon^2}\left(\Delta \partial_u W_{\Omega_{int},\Omega_{ext}}(u) + \left(\triangle u - \frac{1}{\epsilon^2}\partial_u W_{\Omega_{int},\Omega_{ext}}(u,x)\right)\partial_{uu}W_{\Omega_{int},\Omega_{ext}}(u,x)\right) \quad (14)$$

Let us denote by u_ϵ the solution of (14) with initial condition u_0 of the form $u_0 = q(\text{dist}(x,\Omega_0)/\epsilon)$, where the initial set Ω_0 is assumed to satisfy $\Omega_1 \subset \Omega_0 \subset \Omega_2$. The stationary limit of $u_\epsilon(x,t)$ as $t \to \infty$ is expected to be of the form $q(\text{dist}(\Omega_\epsilon^*,x)/\epsilon)$, for some Ω_ϵ^* approximating (11) as ϵ goes to zero. For numerical purposes, we assume that Ω_{ext} is contained in the fixed box $Q = [-1/2, 1/2]^d$ and we look for periodic solutions of the partial differential equation (14). Moreover we choose the potentials W_{int} and W_{ext} as follows:

$$W_{int}(s) = \begin{cases} \frac{1}{2}s^2(1-s)^2 & \text{if } s \geq \frac{1}{2}, \\ 10(s-0.5)^4 + 1/32 & \text{otherwise} \end{cases}, \quad W_{ext}(s) = \begin{cases} \frac{1}{2}s^2(1-s)^2 & \text{if } s \leq \frac{1}{2}, \\ 10(s-0.5)^4 + 1/32 & \text{otherwise} \end{cases}.$$

Our scheme is based on a splitting method which takes advantage of the periodicity of u_ϵ to solve the bi-laplacian part by Fourier's method (see for instance [7]). More precisely, the value $u_\epsilon(x,t_n)$ at time $t_n = t_0 + n\delta t$ is approximated by

$$u_\epsilon^P(x,t_n) = \sum_{\max_{1 \leq i \leq d}|p_i| \leq P} u_{\epsilon,p}(t_n)e^{2i\pi p \cdot x}.$$

In a first step, we set

$$u_\epsilon^P(x,t_n+1/2) = \sum_{\max_{1 \leq i \leq d}|p_i| \leq P} u_{\epsilon,p}(t_n+1/2)e^{2i\pi p \cdot x},$$

with

$$u_{\epsilon,p}(t_n+1/2) = u_{\epsilon,p}(t_n)e^{-16\pi^4\delta t\,|p|^4}.$$

We then integrate all the other terms explicitly :

$$u_\epsilon^P(x,t_n+1) = u_\epsilon^P(x,t_n+1/2) + \delta t R(u_\epsilon^P(x,t_n+1/2)),$$

9

with

$$R(u) = \frac{1}{\epsilon^2} \left(\Delta \partial_u W_{\Omega_{int},\Omega_{ext}}(u) + \left(\triangle u - \frac{1}{\epsilon^2} \partial_u W_{\Omega_{int},\Omega_{ext}}(u,x) \right) \partial_{uu} W_{\Omega_{int},\Omega_{ext}}(u,x) \right).$$

Let us remark that the first step is performed by fast Fourier transform, with a computational cost of order $O(P^d \ln(P))$. Numerically, we observed that the condition $\delta_t \leq \min \left(M \delta_x^2 \epsilon^2, M^2 \epsilon^4 \right)$ is sufficient for the stability of the algorithm, where $\delta_x = \frac{1}{P}$ and $M = \left[\sup_{t \in [0,1]} \left\{ W''(t) \right\} \right]^{-1}$.

5 Comparative evaluation of the three optimization methods

5.1 Description of the tests cases

We proceed as follows to validate our numerical optimization methods. In a first series of experiments, we evaluate the accuracy of the phase field method by comparing it to the convex-restricted method. The objective is to determine if the phase field method can compete with a reference technique to extract the optimal shape. Therefore, we evaluate the global $\int \kappa^2$ value for both methods, and we check how spatial constraints are satisfied by both.

Since the phase field approach, while generic, is very competitive with the reference method, we run a second series of experiments to compare how the GMC method is close to the phase field approach for evaluating the curvature field of the digitized shapes.

For our experiments we use several types of digital shapes (see Figure 5 and Figure 6), which are all obtained through digitization of well known euclidean shapes (disks, ellipses, polygons,...). Input data is therefore a simple digital contour. The digitization constraint is then a one pixel wide band around the former contour. Due to the restriction to convex data of the first series of experiments, the former pixel band is replaced with two convex polygons: the inner polygon is the convex hull of the interior points and the outer polygon is the maximal translation toward exterior points of the inner polygon edges.

More experiments and detailed results can be found at `http://www.lama.univ-savoie.fr/~oudet/Willmore/experiments.html`.

5.2 Phase field versus convex regularization

We start the evaluation of our three different approaches by a comparison between the convex and phase field methods. In the very simple case of convex contours, as it has been reported in section 3, our regularization procedure reduces to a convex programming problem. To compare the efficiency and the reliability of the methods we use the following protocol. Assume that each method produces a discrete sequence of points (P_n) which describes a polygonal approximation of an optimal convex curve. By definition, the energy associated to a polygonal line is always infinite. Thus the first step of our comparison is to approximate those lines by contours of finite energies. The following steps describe an approach which

is very close from the one introduced in section 3 which constructs an approximation by a sequence of arcs of circles :

1. Associate to (P_n) the support function of its convex hull by

$$h_{(P_n)}(\theta) = \sup_n P_n \cdot \nu(\theta)$$

2. Evaluate $h_{(P_n)}$ on a grid of S^1 of size N_g to produce a set of values h_g

3. Look for an optimal sequence of positive radius of curvature (R_i) of length N_c and a translation τ which are optimal in the least square sense:

$$((R_i), \tau) = \arg\min ||L(((R_i), \tau)) - h_g||^2$$

under the constraints (6) where L is the linear operator of evaluation of the associated support function at the angles of the grid of S^1.

4. Associate to $((R_i), \tau)$ its support function h.

We apply the above steps for the output contours of both methods. Let us call h_{pf} and h_c the support functions obtained by the previous approximation with $N_g = 1e3$ and $N_c = 4e2$. We made intensive computations on the test cases described in section 5.1. Whereas the phase field method always converges to a local optimal curve, it happens that the convex approach was not able to identify an admissible curve. This bad behavior of the convex method comes from the fact that the convex regularization of the constraints may lead to very close curves. Moreover, in the case of simple polygons, the curvature may change dramatically rapidly with respect to its angular parametrization. As a consequence, the equally spaced discretization of S^1 that we first implemented was not efficient in those singular case. To overcome this difficulty we adapt the sampling points of S^1 to the optimal locations of knots in the interpolation of $(h_{in} + h_{ext})/2$ (see [18] for the details of the algorithm).

We present in tables 1, 2 and 3 the results obtained by the two methods. Figure 3 shows the optimal curves obtained by both methods on three test cases. The first and third test cases present similar results while the second illustrates the existence of critical curves obtained by the phase field method which are not global minimizer. As expected, the optimal curves are similar but the convex solution is better from the point of view of the constraint satisfaction and of the cost functional on simple examples (see columns 4 to 6 of tables 1 and 2). More surprisingly, the phase field approach is able to produce a very stable approximation of optimal curve : the l_2 norm of the difference (see the third columns) of the two support functions is always less than 3%. This good behavior illustrates that the phase field approach under the stiff constraints of the interior and exterior domains is able to avoid most of none-optimal stationary curves. Of course the price to pay is a small lost of precision with respect to the satisfaction of the constraints. The last examples of table 3 have to be consider as difficult problems since the radius of curvature of the constraints are very irregular. As a consequence, both algorithms are not able to identify completely admissible sets. Nevertheless, the phase field approach is still able to produce in some cases smooth curves with smaller energies than those produced by the convex method. Those bad results of the convex approach are explained by the fact that the interior/projected conjugate gradient algorithm spends all its computational time to try to satisfy the constraints. Once again, those stiff test cases illustrate the robustness of the phase field regularization.

Shape	$\min \frac{|h_{in}-h_{ext}|}{||h_{in}||_\infty}$	$\frac{||h_{pf}-h_c||_2}{||h_c||_2}$	e_{pf}	e_c	$\frac{V_c-V_{pf}}{V_c}$
Circle fu ($r = 12$)	0.006723	0.008741	0.001688	0.000000	-0.012655
Circle fu ($r = 24$)	0.002773	0.004000	0.002177	0.000000	-0.005416
Ellipse fu $a = 12$, $b = 4$, $\theta = 0$	0.006531	0.030307	0.020758	0.000012	-0.005923
Ellipse fu $a = 12$, $b = 4$, $\theta = 10$	0.007899	0.029439	0.021499	0.000000	-0.004685
Ellipse fu $a = 12$, $b = 4$, $\theta = 20$	0.007924	0.027019	0.016129	0.000002	-0.022688
Ellipse fu $a = 12$, $b = 4$, $\theta = 30$	0.006707	0.022180	0.018000	0.000000	-0.008816
Ellipse fu $a = 12$, $b = 4$, $\theta = 40$	0.005446	0.024468	0.017500	0.000000	-0.005152
Ellipse fu $a = 12$, $b = 4$, $\theta = 50$	0.005543	0.025622	0.018817	0.000001	-0.004174
Ellipse fu $a = 12$, $b = 4$, $\theta = 60$	0.007812	0.024553	0.013515	0.000000	-0.012134
Ellipse fu $a = 12$, $b = 4$, $\theta = 70$	0.007703	0.027735	0.020931	0.000000	-0.002501
Ellipse fu $a = 12$, $b = 4$, $\theta = 80$	0.005296	0.027606	0.020148	0.000004	-0.008771
Ellipse fu $a = 24$, $b = 8$, $\theta = 0$	0.002090	0.014748	0.010894	0.000000	-0.003076
Ellipse fu $a = 24$, $b = 8$, $\theta = 10$	0.001638	0.014034	0.010657	0.000003	-0.002341
Ellipse fu $a = 24$, $b = 8$, $\theta = 20$	0.002265	0.013688	0.009783	0.000000	0.003265
Ellipse fu $a = 24$, $b = 8$, $\theta = 30$	0.003278	0.013673	0.012081	0.000000	0.006929
Ellipse fu $a = 24$, $b = 8$, $\theta = 40$	0.002229	0.010485	0.009391	0.000001	0.005319
Ellipse fu $a = 24$, $b = 8$, $\theta = 50$	0.001800	0.009980	0.007984	0.000003	0.000017
Ellipse fu $a = 24$, $b = 8$, $\theta = 60$	0.002443	0.010565	0.010077	0.000000	0.008624
Ellipse fu $a = 24$, $b = 8$, $\theta = 70$	0.002150	0.014058	0.011562	0.000000	0.007921
Ellipse fu $a = 24$, $b = 8$, $\theta = 80$	0.002341	0.013020	0.009313	0.000000	0.002433

Table 1: Phase field versus convex regularization, first set of test cases. e_{pf} stands for $\frac{\max(|h_{in}-h_{pf}|_+, |h_{pf}-h_{ext}|_+)}{||h_{in}||_\infty}$ and e_c is defined in an analogous way.

5.3 Numeric evaluation of the curvature estimators

We compared numerically the closeness of the curvature fields extracted by the GMC method and the phase field method on various shapes at two different resolutions. The error measures are summed up on Table 4. Plots of curvature fields as well as the phase field reconstruction are given on Figure 5 and Figure 6. We also included the curvature field of the euclidean shape before digitization. Notice that the euclidean shape is generally not the optimal shape for minimizing Willmore energy. Nevertheless they share many features such as smoothness and number of position of extremal points. Moreover, by definition of the digital constraints those shapes are geometrically close.

Regarding the evaluation of curvature fields obtained from GMC method and the phase field method we first notice that extremal points are consistently localized with respect to the original shape. Curvature fields of both methods are numerically close for disks and ellipses and get closer as the resolution gets finer. On the other hand the curvature field obtained by the phase field approach is far away from the original shape when considering polygons. This bad behavior is related to the fact that the Willmore energy is not relevant for extracting shapes with non smooth curvature field. In this context the GMC algorithm has a more natural output because it has a pre-processing which locates linear parts of the

Shape	$\min \frac{\|h_{in}-h_{ext}\|}{\|h_{in}\|_\infty}$	$\frac{\|h_{pf}-h_c\|_2}{\|h_c\|_2}$	e_{pf}	e_c	$\frac{V_c-V_{pf}}{V_c}$
Circle ($r=12$)	0.006705	0.010434	0.001678	0.000001	-0.014405
Circle ($r=24$)	0.002319	0.005601	0.001745	0.000001	-0.007997
Ellipse $a=12$, $b=4$, $\theta=0$	0.004563	0.028657	0.020249	0.000027	0.000086
Ellipse $a=12$, $b=4$, $\theta=10$	0.007800	0.029209	0.021227	0.000005	-0.007934
Ellipse $a=12$, $b=4$, $\theta=20$	0.010032	0.028470	0.018518	0.000000	-0.002961
Ellipse $a=12$, $b=4$, $\theta=30$	0.005530	0.024014	0.017747	0.000000	-0.003305
Ellipse $a=12$, $b=4$, $\theta=40$	0.012394	0.025144	0.013271	0.000000	-0.014452
Ellipse $a=12$, $b=4$, $\theta=50$	0.012394	0.025145	0.013183	0.000000	-0.014767
Ellipse $a=12$, $b=4$, $\theta=60$	0.005530	0.024028	0.017502	0.000000	-0.004026
Ellipse $a=12$, $b=4$, $\theta=70$	0.010029	0.028594	0.018565	0.000000	-0.002791
Ellipse $a=12$, $b=4$, $\theta=80$	0.007796	0.029245	0.021235	0.000000	-0.007462
Ellipse $a=24$, $b=8$, $\theta=0$	0.001506	0.014545	0.010824	0.000043	-0.003217
Ellipse $a=24$, $b=8$, $\theta=10$	0.003226	0.014552	0.010127	0.000000	-0.004513
Ellipse $a=24$, $b=8$, $\theta=20$	0.002676	0.014434	0.010861	0.000000	-0.002475
Ellipse $a=24$, $b=8$, $\theta=30$	0.002082	0.014245	0.008439	0.000005	-0.003455
Ellipse $a=24$, $b=8$, $\theta=40$	0.002829	0.011887	0.007807	0.000000	-0.003064
Ellipse $a=24$, $b=8$, $\theta=50$	0.002826	0.011848	0.007825	0.000000	-0.002690
Ellipse $a=24$, $b=8$, $\theta=60$	0.002082	0.014284	0.008395	0.000004	-0.003454
Ellipse $a=24$, $b=8$, $\theta=70$	0.002675	0.014606	0.010919	0.000000	-0.002311
Ellipse $a=24$, $b=8$, $\theta=80$	0.003229	0.014581	0.010129	0.000002	-0.004325

Table 2: Phase field versus convex regularization, second set of test cases. e_{pf} stands for $\frac{\max(|h_{in}-h_{pf}|_+, |h_{pf}-h_{ext}|_+)}{\|h_{in}\|_\infty}$ and e_c is defined in an analogous way.

boundary. This avoids spurious inflexion points which have been observed in phase field reconstruction (see Figure 6 bottom row). A side effect of GMC method is that it preserves convexity.

From a computational cost point of view, the three methods are not equivalent. The GMC method is the fastest (at most 0.1 second for the presented experiments). The phase field method requires computations on grids much finer than the digital shape to enforce the constraints. Therefore computation times take several minutes.

6 Conclusion

We have presented three different methods to address the regularization of digital contours. They are based on the minimization of Willmore energy with specific constraints. The first method limited to convex sets is a reliable numeric scheme for solving this problem and was therefore used as a ground truth for the others. Although the phase field method may fall into local minima it appears to be a very good approximation of optimal shapes. Moreover, the latter method is much more flexible and is adapted to real world data. Finally, we have compared the phase field method with the GMC method, which only approximates

the minimization problem. Experiments have shown that the GMC method gives a good approximation of the curvature field obtained by the phase field reconstruction, in the case of smooth shapes digitization. For shapes containing polygonal parts, the GMC approach gives more natural results since it relaxes in these parts the curvature regularity imposed by the Willmore model.

Two perspectives to this work seem very promising. First of all, the constrained phase field formulation is naturally extensible to 3D shapes. We have started to work on this extension, as displayed on Figure 4. An interesting point is that the convergence is fast (only a few iterations are necessary). Secondly, we would like to mix the pre-processing step of GMC method in phase field reconstruction. This pre-processing could thus detect linear parts and vertices of the original shape, and then marks them specifically so that they are treated differently during the phase field reconstruction. By this way, angular features of shapes could be preserved in the elsewhere smooth reconstruction.

A Proof of Γ-convergence for the penalized perimeter

In this section, we etablish the Γ-convergence of $P_{\epsilon,\Omega_{int},\Omega_{ext}}$ to $c_W P_{\Omega_{int},\Omega_{ext}}$.

Definition A.1 *Let X be a banach space. A sequence $F_\epsilon : X \to \bar{\mathbb{R}}$ is said to Γ-converge to $F : X \to \bar{\mathbb{R}}$ in X if for all u in X,*

- *If $u_\epsilon \to u$, then*

$$F(u) \leq \liminf F_\epsilon(u_\epsilon).$$

- *There exists a sequence $u_\epsilon \to u$ such as*

$$\limsup F_\epsilon(u_\epsilon) \leq F(u).$$

In this paper, we take $X = L^1(\mathbb{R}^d)$ and introduce a lower semi-continuous extension of $P_{\Omega_{int},\Omega_{ext}}$ in $L^1(\mathbb{R}^d)$. For all $u \in L^1(\mathbb{R}^d)$, we then define $P_{\Omega_{int},\Omega_{ext}}(u)$ as follow

$$P_{\Omega_{int},\Omega_{ext}}(u) = \begin{cases} |Du|(\mathbb{R}^d) & \text{if } u = \chi_\Omega \text{ and } \Omega_{int} \subset \Omega \subset \Omega_{ext} \\ +\infty & \text{otherwise,} \end{cases}.$$

where

$$|Du|(\mathbb{R}^d) = \sup\left\{ \int_{\mathbb{R}^d} u \ \text{div} \, g dx \ ; \ g \in \mathcal{D}(\mathbb{R}^d, \mathbb{R}^d) \right\},$$

and $\mathcal{D}(\mathbb{R}^d, \mathbb{R}^d)$ denotes the set of $C^\infty(\mathbb{R}^d, \mathbb{R}^d)$ functions with compact support on $\mathbb{R}^d$. Note that when $u \in W^{1,1}(\mathbb{R}^d)$, $|Du|$ coincides with the L^1-norm of ∇u and if $u = \chi_\Omega$, then $|Du|$ coincides with the perimeter of Ω. Moreover $v \to |Dv|(\mathbb{R}^d)$ is lower semi-continuous in $L^1(\mathbb{R}^d)$ topology.

Theorem A.2 *Assume that Ω_{int} and Ω_{ext} are two given smooth and closed subsets of $\mathbb{R}^d$ such as $\Omega_{int} \subset \Omega_{ext}$ and $dist(\partial\Omega_{int}, \partial\Omega_{ext}) > 0$. Assume that W is a positive and continuous*

double-well potential with wells located at 0 and 1 such that $W(s) = 0$ if and only if $s \in \{0, 1\}$. Assume also that W_{int} and W_{ext} are two continuous potentials satisfying assumption $(H1)$ defined in section 4. Then, the sequence $P_{\epsilon, \Omega_{int}, \Omega_{ext}}$ Γ-converges to $c_W P_{\Omega_{int}, \Omega_{ext}}$ in $L_1(\mathbb{R}^d)$ topology.

Proof

i) *Liminf inequality :*

Let (u_ϵ) be a sequence of functions converging to u in $L^1(\mathbb{R}^d)$. Let us prove that

$$P_{\Omega_{int}, \Omega_{ext}}(u) \leq \liminf P_{\epsilon, \Omega_{int}, \Omega_{ext}}(u_\epsilon).$$

As $P_{\epsilon, \Omega_{int}, \Omega_{ext}} \geq 0$, it is not restrictive to assume that the $\liminf$ of $P_{\epsilon, \Omega_{int}, \Omega_{ext}}(u_\epsilon)$ is finite. Thus, we can extract a subsequence (u_{ϵ_h}) such that

$$\lim_{h \to \infty} P_{\epsilon_h, \Omega_{int}, \Omega_{ext}}(u_{\epsilon_h}) = \liminf_{\epsilon \to 0} P_{\epsilon, \Omega_{int}, \Omega_{ext}}(u_\epsilon) \in \mathbb{R}.$$

Since

$$\begin{cases} \int_{\Omega_{int}} W_{int}(u_{\epsilon_h}) dx \leq \epsilon_h P_{\epsilon_h, \Omega_{int}, \Omega_{ext}}(u_{\epsilon_h}) \\ \int_{\mathbb{R}^d \setminus \Omega_{ext}} W_{ext}(u_{\epsilon_h}) dx \leq \epsilon_h P_{\epsilon_h, \Omega_{int}, \Omega_{ext}}(u_{\epsilon_h}) \\ \int_{\Omega_{ext} \setminus \Omega_{int}} W(u_{\epsilon_h}) dx \leq \epsilon_h P_{\epsilon_h, \Omega_{int}, \Omega_{ext}}(u_{\epsilon_h}), \end{cases}$$

Fatou's Lemma implies that $\int_{\Omega_{int}} W_{int}(u) dx = 0$, $\int_{\mathbb{R}^d \setminus \Omega_{ext}} W_{ext}(u) dx = 0$ and $\int_{\Omega_{ext} \setminus \Omega_{int}} W(u) dx = 0$. By assumptions on potentials W, W_{int} and W_{ext}, it appears that

$$u(x) \in \begin{cases} \{1\} & \text{a.e. in } \Omega_{int}, \\ \{0\} & \text{a.e. in } \mathbb{R}^d \setminus \Omega_{ext}, \\ \{0, 1\} & \text{a.e. in } \Omega_{ext} \setminus \Omega_{int}. \end{cases}$$

Hence, up to some negligible set, u is a characteristic function χ_Ω for some Borel set $\Omega \subset \mathbb{R}^d$ satisfying $\Omega_{int} \subset \Omega \subset \Omega_{ext}$. Using Cauchy's inequality, it holds

$$\begin{aligned} P_{\epsilon, \Omega_{int}, \Omega_{ext}}(u_{\epsilon_h}) & \geq \int_{\mathbb{R}^d} \left[\frac{\epsilon_h |\nabla u_{\epsilon_h}|^2}{2} + \frac{1}{\epsilon_h} W(u_{\epsilon_h}) \right] dx \text{ because } W_{int} \geq W \text{ and } W_{ext} \geq W \\ & \geq \int_{\mathbb{R}^d} \left[\frac{\epsilon_h |\nabla u_{\epsilon_h}|^2}{2} + \frac{1}{\epsilon_h} \tilde{W}(u_{\epsilon_h}) \right] dx \text{ with } \tilde{W}(s) = \min\{W(s), \sup_{s \in [0,1]} W(s)\} \\ & \geq \int_{\mathbb{R}^d} \sqrt{2\tilde{W}(u_{\epsilon_h})} |\nabla u_h| dx = \int_{\mathbb{R}^d} |\nabla [\phi(u_{\epsilon_h})]| dx = |D[\phi(u_{\epsilon_h})]|(\mathbb{R}^d), \end{aligned}$$

where $\phi(s) = \int_0^s \sqrt{2\tilde{W}(t)} dt$. Since ϕ is a Lipschitz function (because $\tilde{W}$ is bounded), $\phi(u_\epsilon)$ converges in $L^1(\mathbb{R}^d)$ to $\phi(u)$. Using the lower semicontinuity of $v \to |Dv|(\mathbb{R}^d)$, we obtain

$$\lim_{h \to +\infty} P_{\epsilon_h, \Omega_{int}, \Omega_{ext}}(u_{\epsilon_h}) \geq \liminf_{h \to +\infty} |D\phi(u_{\epsilon_h})|(\mathbb{R}^d) \geq |D\phi(u)|(\mathbb{R}^d).$$

As $\phi(u) = \phi(\chi_\Omega) = c_W \chi_\Omega = c_W u$, we finally obtain the $\liminf$ inequality.

ii) *Limsup inequality :*

Let u be a function in $L_1(\mathbb{R}^d)$. We prove below the existence of a sequence (u_ϵ) converging to u such as

$$\limsup P_{\epsilon,\Omega_{int},\Omega_{ext}}(u_\epsilon) \leq P_{\Omega_{int},\Omega_{ext}}(u).$$

We can assume that $P_{\Omega_{int},\Omega_{ext}}(u)$ is finite, this means that $u = \chi_\Omega$ for some bounded open set Ω satisfying $\Omega_{int} \subset \Omega \subset \Omega_{ext}$ with smooth boundary. Introduce the sequence

$$u_\epsilon(x) = q\left(\frac{\text{dist}(x,\Omega)}{\epsilon}\right),$$

where the profile q is defined by (13). Like in section 4, $\text{dist}(x,\Omega)$ denotes the signed distance function to the set Ω. Note that by the definition of q, u_ϵ converges to u. As q is clearly decreasing and $q(0) = 1/2$, it follows that

- The function $\text{dist}(x,\Omega)$ is negative on Ω_{int}, thus $u_\epsilon(x) \geq \frac{1}{2}$ on Ω_{int} and then

$$W_{\epsilon,\Omega_{int},\Omega_{ext}}(u_\epsilon(x),x) = W_{int}(u_\epsilon(x)) = W(u_\epsilon(x)), \quad \text{for all } x \in \Omega_{int},$$

- The function $\text{dist}(x,\Omega)$ is positive on $\mathbb{R}^d \setminus \Omega_{ext}$, thus $u_\epsilon(x) \leq \frac{1}{2}$ on $\mathbb{R}^d \setminus \Omega_{ext}$ and

$$W_{\epsilon,\Omega_{int},\Omega_{ext}}(u_\epsilon(x),x) = W_{ext}(u_\epsilon(x)) = W(u_\epsilon(x)), \quad \text{for all } x \in \mathbb{R}^d \setminus \Omega_{ext}.$$

Hence, by co-area formula, we estimate

$$\begin{aligned}
P_{\epsilon,\Omega_{int},\Omega_{ext}}(u_\epsilon) &= \int_{\mathbb{R}^d}\left[\frac{\epsilon|\nabla u_\epsilon|^2}{2} + \frac{1}{\epsilon}W(u^\epsilon)\right]dx = \frac{1}{\epsilon}\int_{\mathbb{R}^d}\left[\frac{q'(d(x,\Omega)/\epsilon)^2}{2} + W(q(d(x,\Omega)/\epsilon))\right]dx \\
&= \frac{1}{\epsilon}\int_{\mathbb{R}}g(s)\left[\frac{q'(s/\epsilon)^2}{2} + W(q(s/\epsilon))\right]ds = \int_{\mathbb{R}}g(\epsilon t)\left[\frac{q'(t)^2}{2} + W(q(t))\right]dt
\end{aligned}$$

where $g(s) = |D\chi_{\{d \leq s\}}|(\mathbb{R}^d)$. By the smoothness of $\partial\Omega$, $g(\epsilon t)$ converges to

$$g(0) = |D\chi_{\text{dist}(x,\Omega)\leq 0}|(R^d) = |D\chi_\Omega|(R^d) = P_{\Omega_{int},\Omega_{ext}}(u),$$

and so

$$\limsup_{\epsilon\to 0} J_{\epsilon,\Omega_{int},\Omega_{ext}}(u_\epsilon) \leq P_{\Omega_{int},\Omega_{ext}}(u)\int_{-\infty}^{+\infty}\left[\frac{1}{2}q'(s)^2 + W(q(s))ds\right].$$

The proof is closed by the following equality

$$\int_{-\infty}^{+\infty}\left[\frac{1}{2}q'(s)^2 + W(q(s))\right]ds = \int_0^1\sqrt{2W(s)}ds = c_W.$$

□

References

[1] G. Alberti. Variational models for phase transitions, an approach via γ-convergence. In *Calculus of variations and partial differential equations (Pisa, 1996)*, pages 95–114. Springer, Berlin, 2000.

[2] L. Ambrosio. Geometric evolution problems, distance function and viscosity solutions. In *Calculus of variations and partial differential equations (Pisa, 1996)*, pages 5–93. Springer, Berlin, 2000.

[3] G. Bellettini. Variational approximation of functionals with curvatures and related properties. *J. Convex Anal.*, 4(1):91–108, 1997.

[4] E. Bretin. *Mouvement par courbure moyenne et méthode de champ de phase.* PhD thesis, Institut polytechnique de Grenoble, 2009.

[5] R. H. Byrd, J. Nocedal, and R. A. Waltz. KNITRO: An integrated package for nonlinear optimization. In *Large-scale nonlinear optimization*, volume 83 of *Nonconvex Optim. Appl.*, pages 35–59. Springer, New York, 2006.

[6] Tony F. Chan, Sung Ha Kang, and Jianhong Shen. Euler's elastica and curvature-based inpainting. *SIAM J. Appl. Math.*, 63(2):564–592 (electronic), 2002.

[7] L.Q. Chen and J. Shen. Applications of semi-implicit fourier-spectral method to phase field equations. *Computer Physics Communications*, 108:147–158, 1998.

[8] X. Chen. Generation and propagation of interfaces for reaction-diffusion equations. *J. Differential Equations*, 96(1):116–141, 1992.

[9] Xinfu Chen, Charlie M. Elliott, Andy Gardiner, and Jennifer Jing Zhao. Convergence of numerical solutions to the Allen-Cahn equation. *Appl. Anal.*, 69(1-2):47–56, 1998.

[10] P.-G. Ciarlet. *Introduction à l'analyse numérique et à l'optimisation.* Sciences Sup. Dunod, Paris, 1998.

[11] F. de Vieilleville, J.-O. Lachaud, and F. Feschet. Maximal digital straight segments and convergence of discrete geometric estimators. *Journal of Mathematical Imaging and Vision*, 27(2):471–502, February 2007.

[12] Qiang Du, Chun Liu, Rolf Ryham, and Xiaoqiang Wang. A phase field formulation of the Willmore problem. *Nonlinearity*, 18(3):1249–1267, 2005.

[13] Qiang Du, Chun Liu, and Xiaoqiang Wang. A phase field approach in the numerical study of the elastic bending energy for vesicle membranes. *J. Comput. Phys.*, 198(2):450–468, 2004.

[14] C. M. Elliott. Approximation of curvature dependent interface motion. In *The state of the art in numerical analysis (York, 1996)*, volume 63 of *Inst. Math. Appl. Conf. Ser. New Ser.*, pages 407–440. Oxford Univ. Press, New York, 1997.

[15] L. C. Evans, H. M. Soner, and P. E. Souganidis. Phase transitions and generalized motion by mean curvature. *Comm. Pure Appl. Math.*, 45(9):1097–1123, 1992.

[16] F. Feschet and L. Tougne. Optimal time computation of the tangent of a discrete curve: Application to the curvature. In *Proc. 8th Int. Conf. Discrete Geometry for Computer Imagery (DGCI'99)*, number 1568 in LNCS, pages 31–40. Springer, 1999.

[17] Craig G. Fraser. Mathematical technique and physical conception in Euler's investigation of the elastica. *Centaurus*, 34(3):211–246, 1991.

[18] P. W. Gaffney and M. J. D. Powell. Optimal interpolation. In *Numerical analysis (Proc. 6th Biennial Dundee Conf., Univ. Dundee, Dundee, 1975)*, pages 90–99. Lecture Notes in Math., Vol. 506. Springer, Berlin, 1976.

[19] M. Kass, A. Witkin, and D. Terzopoulos. Snakes: Active contour models. *International Journal of Computer Vision*, 1(4):321–331, 1988.

[20] B. Kerautret and J.-O. Lachaud. Robust estimation of curvature along digital contours with global optimization. In D. Coeurjolly, I. Sivignon, L. Tougne, and F. Dupont, editors, *Proc. Int. Conf. Discrete Geometry for Computer Imagery (DGCI'2008), Lyon, France*, volume 4992 of *LNCS*, pages 334–345. Springer, April 2008.

[21] B. Kerautret and J.-O. Lachaud. Curvature estimation along noisy digital contours by approximate global optimization. *Pattern Recognition*, 42(10):2265 – 2278, 2009.

[22] J.-O. Lachaud. *Espaces non-euclidiens et analyse d'image : modèles déformables riemanniens et discrets, topologie et géométrie discrète*. Habilitation à diriger des recherches, Université Bordeaux 1, Talence, France, 2006. In french.

[23] J.-O. Lachaud, A. Vialard, and F. de Vieilleville. Fast, accurate and convergent tangent estimation on digital contours. *Image and Vision Computing*, 25(10):1572–1587, October 2007.

[24] L. Modica and S. Mortola. Il limite nella Γ-convergenza di una famiglia di funzionali ellittici. *Boll. Un. Mat. Ital. A (5)*, 14(3):526–529, 1977.

[25] L. Modica and S. Mortola. Un esempio di Γ⁻-convergenza. *Boll. Un. Mat. Ital. B (5)*, 14(1):285–299, 1977.

[26] Matthias Röger and Reiner Schätzle. On a modified conjecture of De Giorgi. *Math. Z.*, 254(4):675–714, 2006.

[27] Reiner Schätzle. Lower semicontinuity of the Willmore functional for currents. *J. Differential Geom.*, 81(2):437–456, 2009.

[28] Reiner Schätzle. The Willmore boundary problem. *Calc. Var. Partial Differential Equations*, 37(3-4):275–302, 2010.

[29] Rolf Schneider. *Convex bodies: the Brunn-Minkowski theory*, volume 44 of *Encyclopedia of Mathematics and its Applications*. Cambridge University Press, Cambridge, 1993.

[30] T. J. Willmore. *Riemannian geometry.* Oxford Science Publications. The Clarendon Press Oxford University Press, New York, 1993.
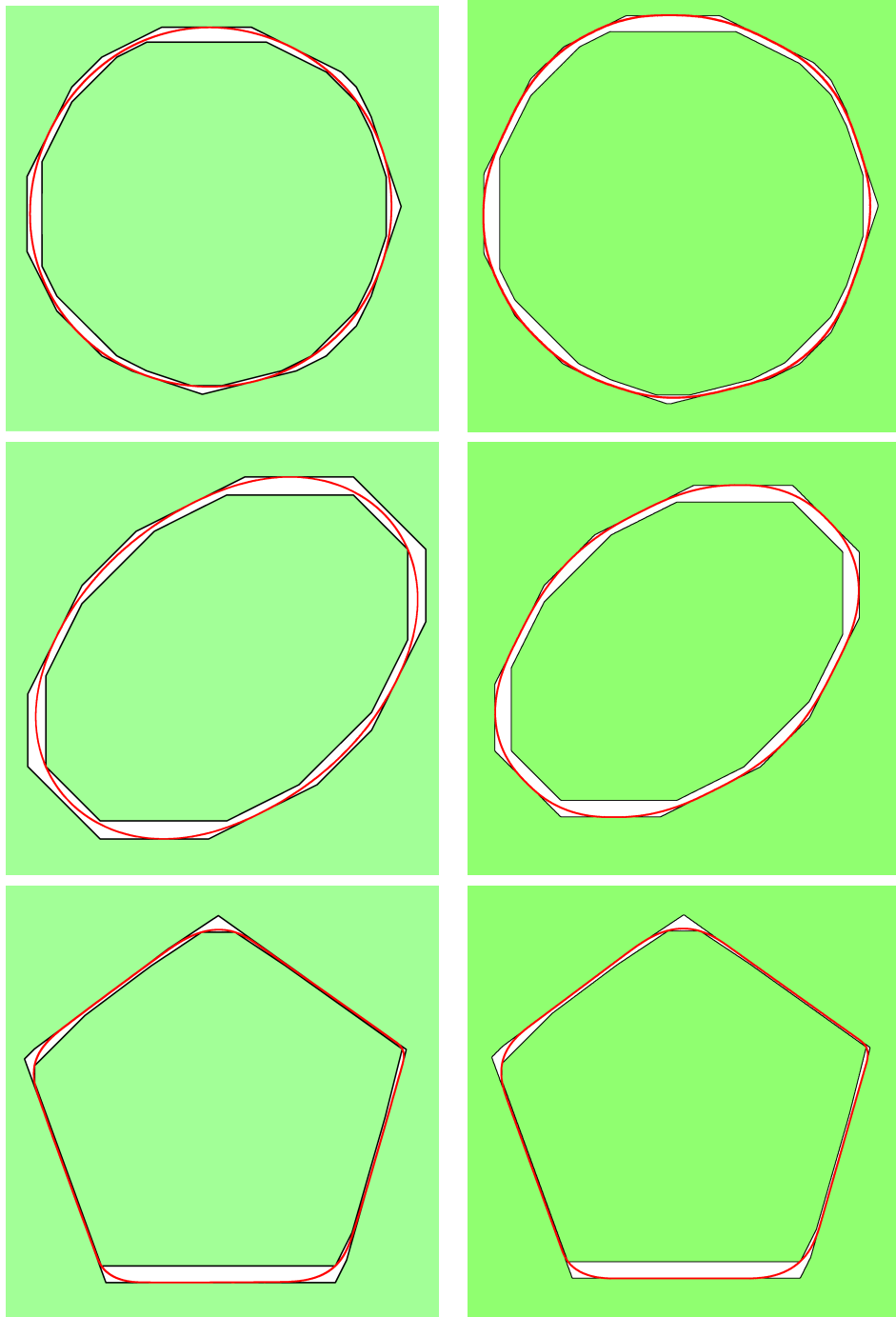
Figure 3: Optimal curves obtained by the convex approach (left column) and phase field method (right column). The first and third rows present similar results while the second illustrates the existence of critical curves obtained by the phase field method which are not global minimizer.

Shape	$\min \frac{|h_{in}-h_{ext}|}{||h_{in}||_\infty}$	$\frac{||h_{pf}-h_c||_2}{||h_c||_2}$	e_{pf}	e_c	$\frac{V_c-V_{pf}}{V_c}$
Triangle $R=12$, $\theta=10$	0.003513	0.023859	0.019938	0.000851	0.003610
Triangle $R=12$, $\theta=20$	0.003739	0.024980	0.021457	0.000575	0.004298
Triangle $R=12$, $\theta=40$	0.003482	0.029507	0.019860	0.000418	0.013267
Triangle $R=12$, $\theta=50$	0.003198	0.022848	0.020171	0.000318	0.001871
Triangle $R=12$, $\theta=70$	0.003383	0.026008	0.022031	0.000445	0.003445
Triangle $R=12$, $\theta=80$	0.003822	0.032327	0.020775	0.000500	0.012414
Triangle $R=24$, $\theta=10$	0.000901	0.011796	0.009539	0.000675	0.002337
Triangle $R=24$, $\theta=20$	0.000445	0.012118	0.010628	0.000880	0.003215
Triangle $R=24$, $\theta=40$	0.000425	0.017871	0.010507	0.000967	0.011385
Pentagon $R=12$, $\theta=0$	0.003317	0.023734	0.019024	0.000292	-0.000549
Pentagon $R=12$, $\theta=10$	0. 004275	0.024006	0.018680	0.000190	-0.001132
Pentagon $R=12$, $\theta=20$	0.002442	0.023517	0.019214	0.000229	-0.000115
Pentagon $R=12$, $\theta=30$	0.004057	0.041961	0.019036	0.000766	0.019678
Pentagon $R=12$, $\theta=40$	0.002520	0.025316	0.019623	0.000503	0.001771
Pentagon $R=12$, $\theta=50$	0.002517	0.025165	0.019796	0.000613	0.001452
Pentagon $R=12$, $\theta=60$	0.002652	0.023625	0.019341	0.000494	-0.000542
Pentagon $R=12$, $\theta=70$	0.002438	0.023528	0.019051	0.000458	-0.000473
Pentagon $R=12$, $\theta=80$	0.004280	0.024005	0.018675	0.000179	-0.001081
Pentagon $R=24$, $\theta=0$	0.001083	0.011721	0.009866	0.000513	0.000152
Pentagon $R=24$, $\theta=10$	0.000791	0.010724	0.008896	0.000358	0.000264
Pentagon $R=24$, $\theta=20$	0.001215	0.014767	0.009490	0.000389	0.003003
Pentagon $R=24$, $\theta=30$	0.000877	0.011685	0.009850	0.000562	0.000629
Pentagon $R=24$, $\theta=40$	0.001001	0.014500	0.010176	0.000128	0.003537
Pentagon $R=24$, $\theta=50$	0.000999	0.011346	0.010462	0.000250	0.000054
Pentagon $R=24$, $\theta=60$	0.000869	0.011748	0.010133	0.000729	0.000528
Pentagon $R=24$, $\theta=70$	0.001204	0.012001	0.009736	0.000437	-0.000670
Pentagon $R=24$, $\theta=80$	0.000786	0.011108	0.008962	0.000373	-0.000211

Table 3: Phase field versus convex regularization, third set of test cases. e_{pf} stands for $\frac{\max(|h_{in}-h_{pf}|_+,|h_{pf}-h_{ext}|_+)}{||h_{in}||_\infty}$ and e_c is defined in an analogous way.
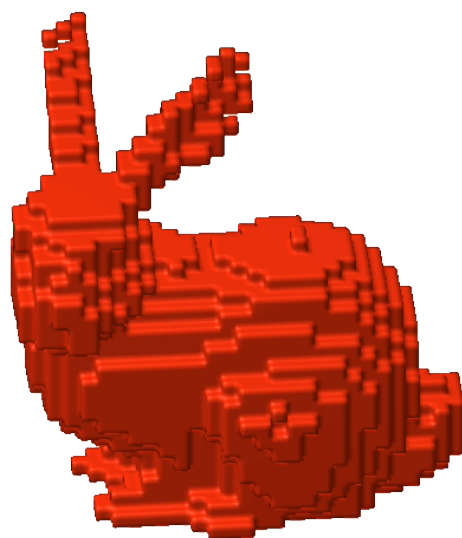
iteration 0
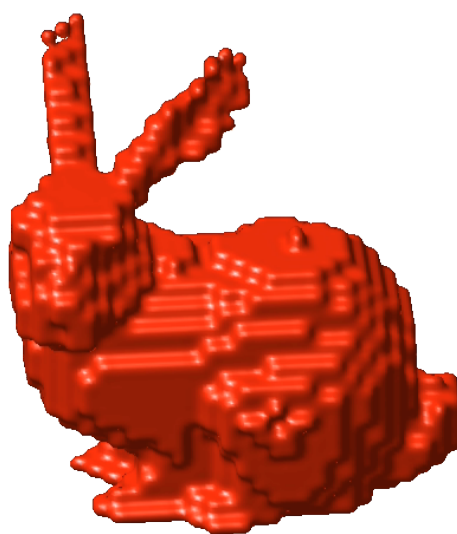
iteration 2
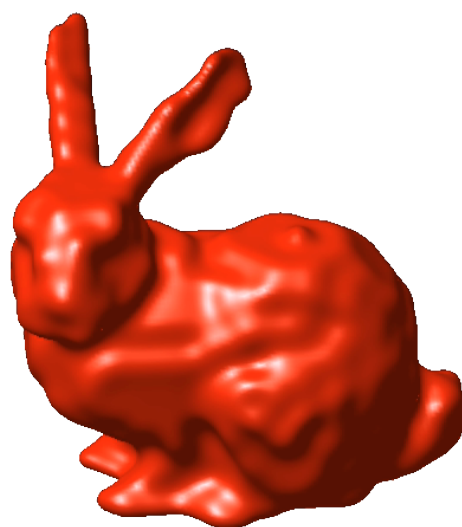
iteration 10
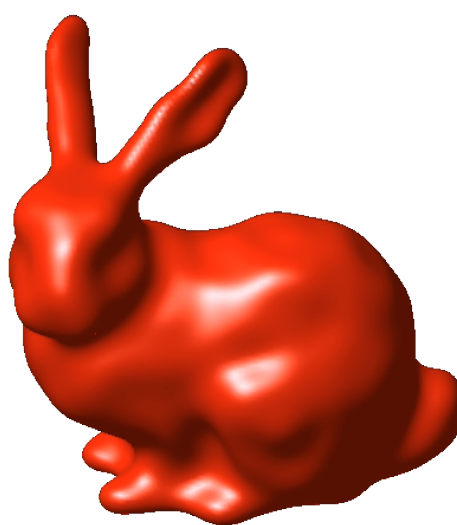
iteration 48

Figure 4: Phase field reconstruction of 3D digital rabbit.

Shape	coarse resolution		fine resolution	
	$\frac{\|\kappa_{gmc}-\kappa_{pf}\|_2}{\|\kappa_{pf}\|_2}$	$\frac{\|\kappa_{gmc}-\kappa_{pf}\|_\infty}{\|\kappa_{pf}\|_\infty}$	$\frac{\|\kappa_{gmc}-\kappa_{pf}\|_2}{\|\kappa_{pf}\|_2}$	$\frac{\|\kappa_{gmc}-\kappa_{pf}\|_\infty}{\|\kappa_{pf}\|_\infty}$
Circle fu ($r = 12$)	0.0442592	0.31289	0.00401175	0.169518
Circle ($r = 12$)	0.0121884	0.220581	0.00216341	0.115145
Ellipse $a = 12, b = 4, \theta = 0$	1.47904	2.69682	0.370295	1.43554
Ellipse $a = 12, b = 4, \theta = 30$	0.21861	0.645565	0.0793507	0.340042
Ellipse $a = 12, b = 4, \theta = 50$	0.105899	0.42965	0.27194	0.726569
Ellipse $a = 12, b = 8, \theta = 0$	0.100187	0.431556	0.0509497	0.350009
Ellipse $a = 12, b = 8, \theta = 30$	0.0413763	0.425344	0.0815066	0.386105
Ellipse $a = 12, b = 8, \theta = 50$	0.0610666	0.278151	0.0541655	0.409225
Flower 3 $R = 11, r = 4, \theta = 0$	0.349944	0.850607	0.139678	0.555303
Flower 3 $R = 11, r = 4, \theta = 30$	0.5012	1.30817	0.570592	1.3973
Flower 3 $R = 11, r = 4, \theta = 50$	0.566741	1.08319	0.942863	2.17071
Flower 5 $R = 16, r = 12, \theta = 10$	0.278245	0.742139	0.428769	2.69516
Flower 5 $R = 16, r = 12, \theta = 40$	0.506603	1.17315	0.347179	1.78096
Pentagon $R = 12, \theta = 0$	0.393705	0.599844	0.847753	1.49237
Pentagon $R = 12, \theta = 30$	0.243533	0.807363	1.49061	2.1423
Triangle $R = 12, \theta = 0$	0.916627	2.0024	2.79765	3.77142
Triangle $R = 12, \theta = 50$	1.44723	1.93351	3.15181	3.00341

Table 4: Normalized error measures in L_2 and L_∞ norms between GMC curvature estimation (κ_{gmc}) and curvature field of phase field reconstruction (κ_{pf}). Tests are made on various shapes obtained by digitization (disk and ellipses, flowers with petals, polygons).
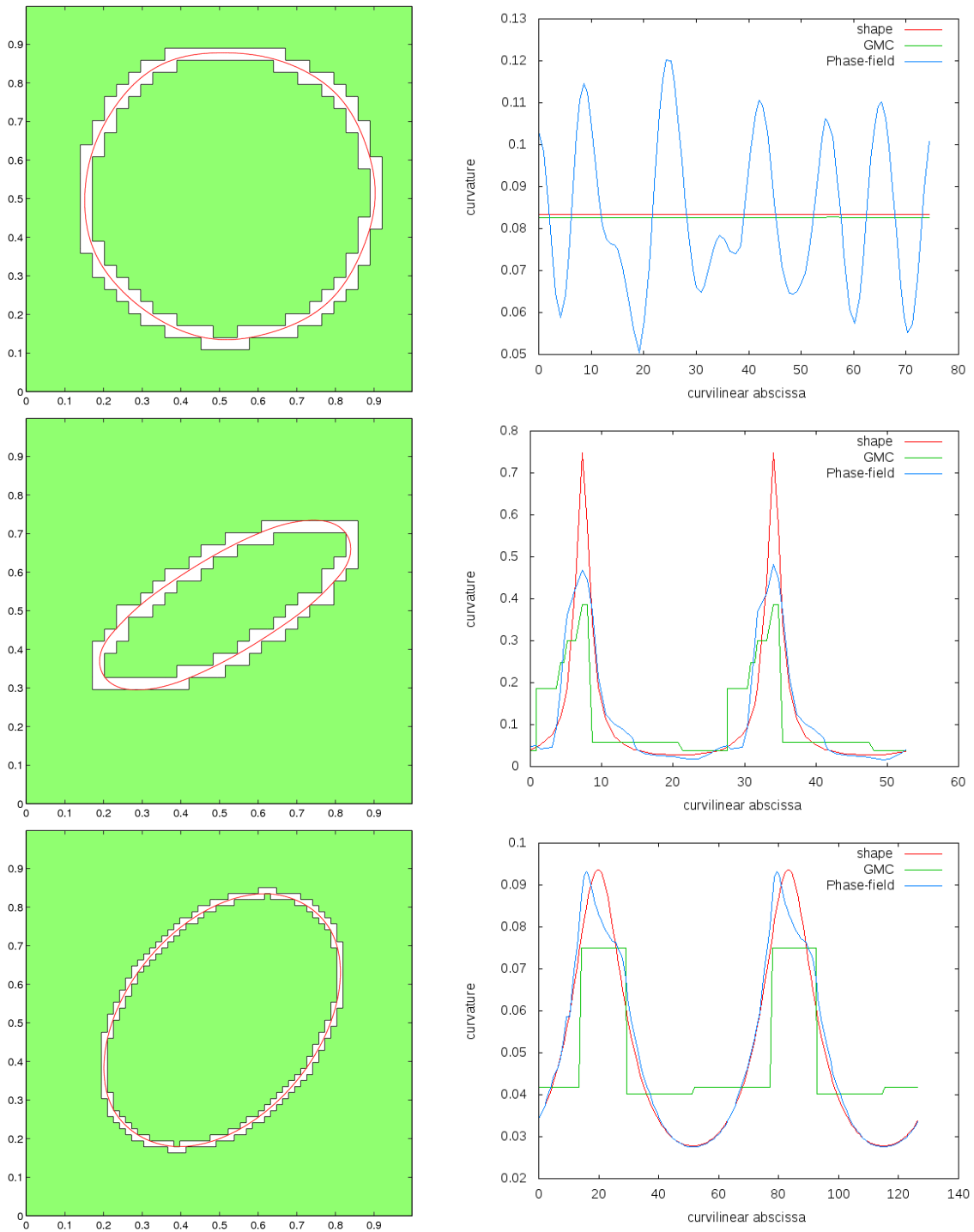
Figure 5: Digital shapes (left: contour as white digital path), phase field reconstruction (left: red curve) and comparison of curvature estimations (right). Top row: Circle fu, $r = 12$. Middle row: Ellipse, $a = 12$, $b = 4$, phase $\theta = 30$. Bottom row: Ellipse (twice finer resolution), $a = 12$, $b = 8$, phase $\theta = 50$.
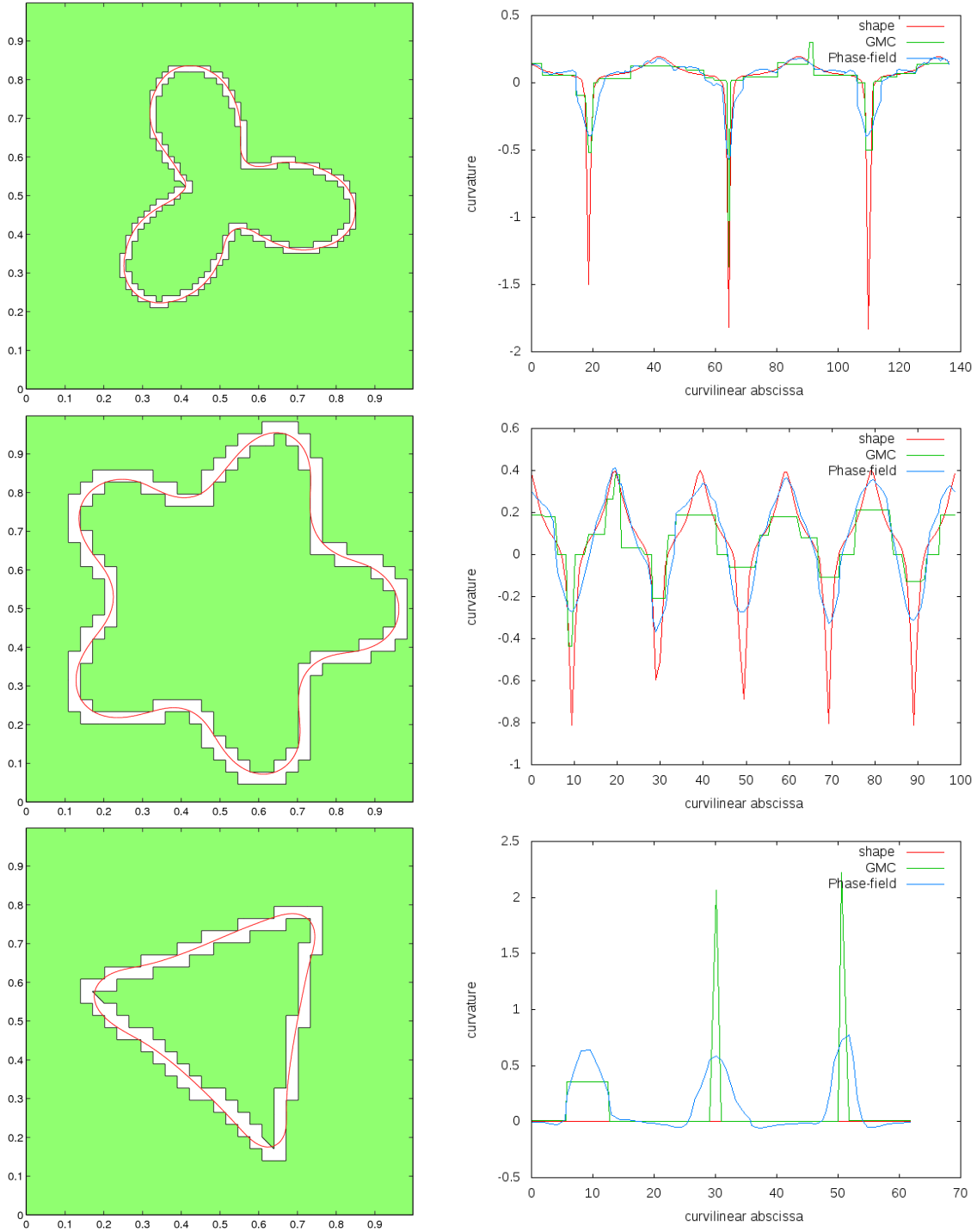
Figure 6: Digital shapes (left: contour as white digital path), phase field reconstruction (left: red curve) and comparison of curvature estimations (right). Top row: Flower with three petals (fine resolution), outer radius $R = 11$, inner radius $r = 4$, phase , $\theta = 30$. Middle row: Flower with five petals (fine resolution), $R = 16$, $r = 12$, $\theta = 10$. Bottom row: Triangle, $r = 12$, $\theta = 50$.